PROCEEDINGS OF SCIENCE

Optimizing Selection Criteria for the CALET Ultra-Heavy Cosmic Ray Analysis

Wolfgang V. Zober,[a,*] **Brian F. Rauch,**[a] **Anthony W. Ficklin**[b] **and Nicholas Cannady**[c] **for the CALET collaboration**

[a] *Department of Physics and McDonnell Center for the Space Sciences, Washington University, St. Louis, MO 63130 USA*

[b] *Department of Physics and Astronomy, Louisiana State University, Baton Rouge, LA 70803 USA*

[c] *CRESST-II/University of Maryland, Baltimore County/NASA Goddard Space Flight Center*

E-mail: wzober@wustl.edu

CALET, the Calorimetric Electron Telescope, launched to the International Space Station in August 2015 and in continuous operation since, has gathered over seven years of data so far. CALET is able to measure cosmic-ray (CR) electrons, nuclei, and gamma rays and with its 27 radiation length deep Total Absorption Calorimeter (TASC), measures particle energy, allowing for the determination of spectra and secondary to primary ratios of the more abundant CR nuclei through $_{28}$Ni, while the main charge detector (CHD) can measure Ultra-Heavy (UH) CR nuclei through $_{40}$Zr. CALET UHCR analyses use a special high duty cycle UH trigger with an expanded geometry that does not require passage through the TASC. To effectively analyze UHCR trigger events, a number of screens and corrections have been developed for the analysis. From time- and position-dependent detector response corrections based on $_{14}$Si and $_{26}$Fe, to an angle-dependent geomagnetic cutoff rigidity selections and minimum deposited energy screens, a number of methods have been explored to optimize UH statistics to varying effect. In this work, we aim to show how these event selection screens and corrections have been developed, how the rigidity screens shown previously by Rauch et al. [1] compare to the newer TASC methodology shown in Zober et al. (2023) [2], and how TASC selections may be used to influence analysis on the full UH-trigger dataset.

38th International Cosmic Ray Conference (ICRC2023)
26 July - 3 August, 2023
instrument Nagoya, Japan

*Speaker

PoS(ICRC2023)089

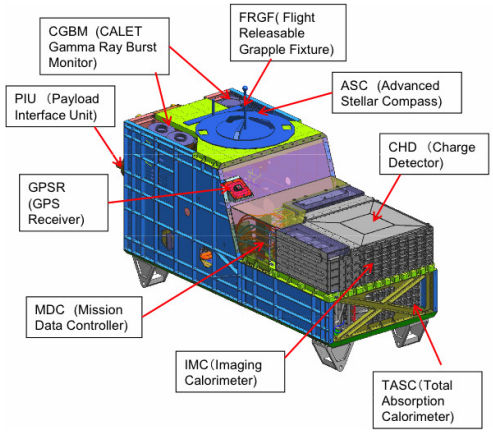

Figure 1(a): CALET instrument package detailing locations of the various CALET subsystems.

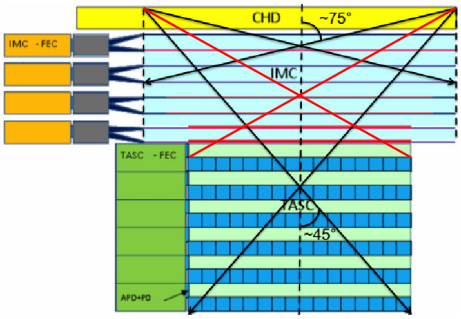

Figure 1(b): CALET side-view showing CHD, IMC, and TASC detector placement with the maximum acceptance angles for detection. The maximum acceptance angle (75°) for the UH trigger analysis is shown in black and in red for the TASC analysis (45°).

1. Introduction

The CALorimetric Electron Telescope (CALET) on the International Space Station (ISS) is a Japanese led astroparticle observatory that was launched on August 19, 2015 and has been collecting scientific data since October 13, 2015. As its name suggests, the main science objective of CALET is to directly measure the total cosmic-ray electron flux (e^-+e^+) to the highest energies (1 GeV to 20 TeV) with the main calorimeter (CAL), shown in the CALET instrument package in Fig. 1a. The calorimeter is also capable of measuring gamma rays (10 GeV to 10 TeV) and cosmic-ray nuclei (up to 1,000 TeV). In addition, there is the CALET Gamma-ray Burst Monitor (CGBM), which can make simultaneous observations with the calorimeter [3].

The main calorimeter instrument is comprised of three detector systems, shown in more detail in a side view in Fig. 1b. At the top is the charge detector (CHD), comprised of an x and a y layer, each having 14 scintillator paddles. The paddles all are 32 mm wide by 10 mm thick by 450 mm long. Below the CHD is the imaging calorimeter (IMC), which is 156.5 mm tall, and made of 8 layers of both x and y scintillating fibers that are 1 mm wide square and 448 mm long. In between the fiber layers of the IMC are a combined 3.0 radiation lengths (X_0) of tungsten arranged such that the first 5 layers are $0.2X_0$ thick and the bottom two are each $1.0X_0$ thick. At the bottom of the instrument stack is the total absorption calorimeter (TASC). This is made of 6 x and y layers of 16 lead tungstate (PWO) scintillator logs. Each of these logs are 19 mm wide, 20 mm tall, and 326 mm long. Combined, these logs give the TASC a depth of $27X_0$. The CHD, along with the IMC, provide the particle charge identification. All three detectors (but primarily the IMC) are utilized for track reconstruction, while the particle energy is determined from the calorimeters, with most of the determination based on TASC measurements.

2. Data

A High-Level Analysis (HLA) dataset has been developed at Louisiana State University (LSU) and Goddard Space Flight Center/University of Maryland - Baltimore County, (GSFC/UMBC). This dataset itself has been given the name Ultra-Heavy Analysis (UHA). The UHA dataset

is written in the ROOT file format like the full CALET Level2 dataset, but organized into a lightweight structure that can be used in different analysis methods. There is a single TTree, containing five branches, each of which is a simple structure of C++ primitive data types. The simplicity of the structure means that, in addition to an analysis in the ROOT C++ framework natively, the data can be read in Python using either the PyROOT package or the uproot package that circumvents ROOT entirely. This data-format features significantly smaller data-files, where a single day of UH trigger data is less than 45 megabytes while a single hour of the Level2 data is on the order of 1 - 2 GB. This means that UHA dataset can read in the entirety of the UH analysis and do full dataset corrections and modifications without the need of scripting or sampling.

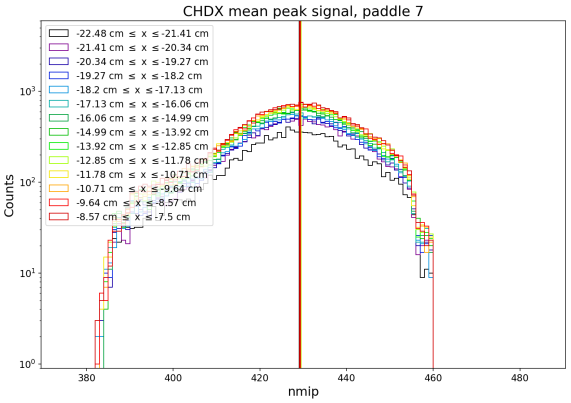

Figure 2: Example peak fitting for part of CHDX paddle 7. Each colored histogram corresponds to a region on the paddle with x=0 as the center of the paddle length. Vertical lines correspond to the identified peak means in the fitting routine for $_{26}$Fe events.

3. Corrections

The CALET instrument has many corrections already applied to the dataset, however these corrections are optimized for the main electron analysis. Since the UH analysis events have significantly different detector signals that vary with Z^2, we need to perform a number of secondary corrections to optimize on the UH region.

3.1 Position-based Corrections

Supplemental corrections to CHD paddle response as a function of longitudinal position are derived by dividing each CHD paddle into 42 segments (with length $\sim$ 1/3 of paddle width). For each individual paddle segments we perform a Gaussian fit on $_{26}$Fe (example in Fig. 2) and $_{14}$Si events to determine the local mean signal for those elements. We then take these local means and find the ratio of the full layer means for both $_{26}$Fe and $_{14}$Si respectively. We then plug these ratios into a scaling function with a hyperbolic tangent function to allow for proportional scaling for elements between $_{14}$Si and $_{26}$Fe and only affected by the nearest of the two outside that range. This provides a smoothly varying CHD signal response for all Z. Equation 1 defines $S(x)$ as the initial signal of an event, Si_{ratio} and Fe_{ratio} as the correction ratios for that event location and Si_{avg} and Fe_{avg} as the full layer means.

$$S(x)_{corr} = S(x)Si_{ratio} + \left[1 + \tanh\left(\frac{1}{40}\left(S(x) - \frac{Si_{avg} + Fe_{avg}}{2}\right)\right)\right] \frac{S(x)Fe_{ratio} - S(x)Si_{ratio}}{2} \quad (1)$$

The validation of this function can be seen in Fig. 3, where Figs. 3a and 3b represent a map of the $_{26}$Fe mean signals in CHDX and CHDY for pre and post correction. We see that there are a number of paddles that read out substantially higher or lower than the full mean, and post correction we get one normalized map. This behavior is also seen in Figures 3c and 3d with $_{14}$Si showing

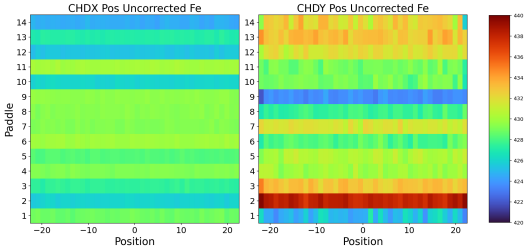

Figure 3(a): Uncorrected $_{26}$Fe map

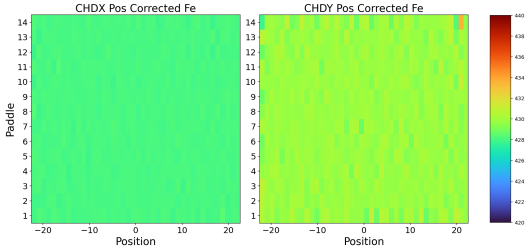

Figure 3(b): Position corrected $_{26}$Fe

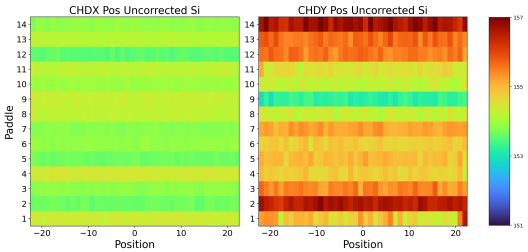

Figure 3(c): Uncorrected $_{14}$Si Map

Figure 3(d): Position corrected $_{14}$Si

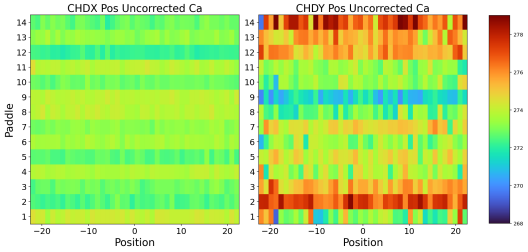

Figure 3(e): Uncorrected $_{20}$Ca means

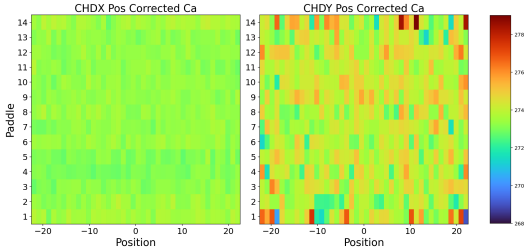

Figure 3(f): $_{20}$Ca means post-correction

somewhat similar behavior. It is noteworthy that the paddles that read out higher and lower do vary from those in $_{26}$Fe, illustrating the need to use more than one element in this correction. We can also explore the effects of this correction on an intermediate element between $_{26}$Fe and $_{14}$Si such as $_{20}$Ca. In Figures 3e and 3f, we can that this correction works fairly well on elements away from the correction peaks, but still leaves some level of noise.

3.2 Time-based Corrections

The time-based corrections are performed similarly, with the "local" steps being defined as increments in time such that there are a minimum 550 $_{26}$Fe events in the final paddle of CHDY for each time step. This results in time correction bins being approximately 3 days in length. It should be noted that this is a significantly smaller subset to perform Gaussian fits on and does lead to some noise in the distributions. Most noise is caused by Poissonian statistics, but other issues caused by obstructions or rotations of the ISS can cause issues here. Some of this noise can go away with a longer event binning, but this would require the equivalent of 2 week observational period.

Figure 4 depicts the before and after for these corrections for $_{26}$Fe. Here in Figures 4a and 4b, we can see how some of the individual paddles vary over time for CHDX and CHDY. In these two plots we can see oscillations in mean peak signal that can be traced back to changes in ISS altitude and thermal control of the CALET instrument. In fact the largest jumps that are seen in these two figures are related a combination of changes in the thermal loop and the calibrations of CALET

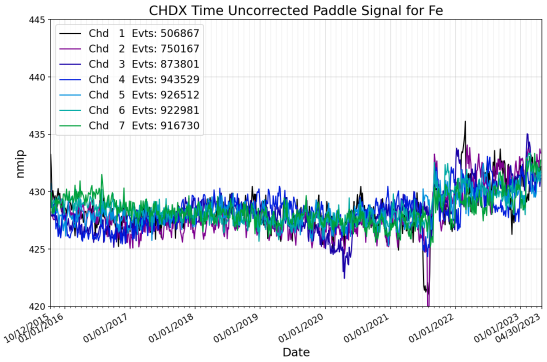

Figure 4(a): Uncorrected $_{26}$Fe signal for CHDX Paddles 1-7.

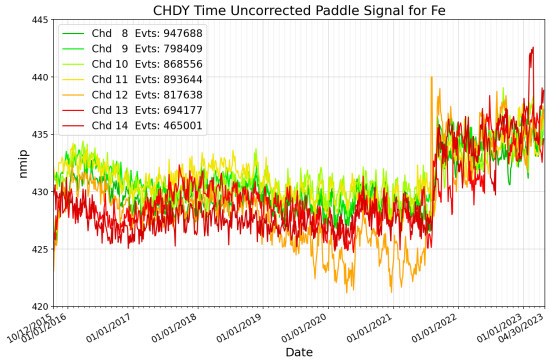

Figure 4(b): Uncorrected $_{26}$Fe Signal for CHDY for paddles 8-14.

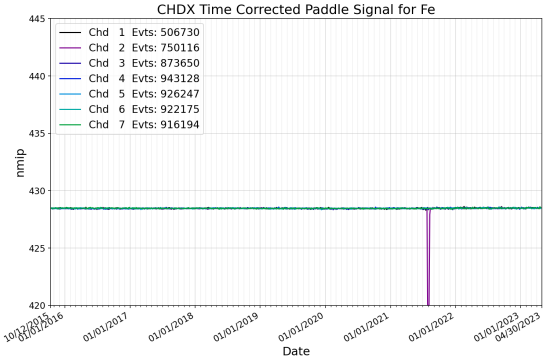

Figure 4(c): Time Corrected signal for CHDX Paddles 1-7.

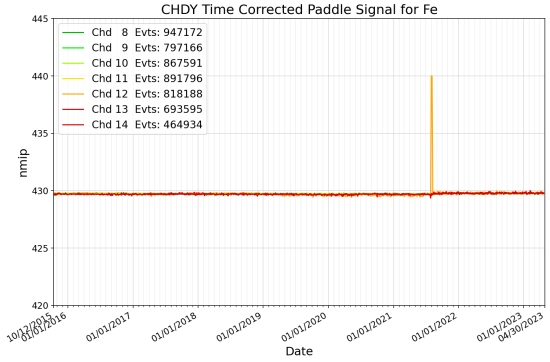

Figure 4(d): Time Corrected signal for CHDY Paddles 8-14.

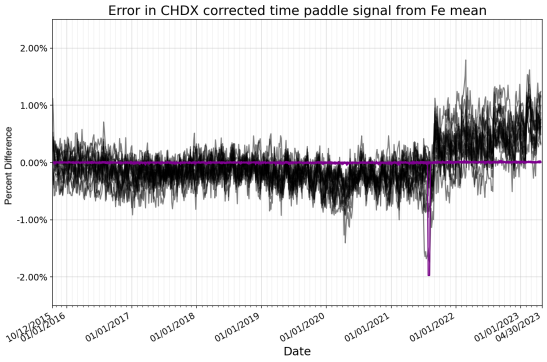

Figure 4(e): Overlay of pre- and post-time corrections for CHDX $_{26}$Fe. Black shows percent error from full layer mean for all paddle means for $_{26}$Fe on CHDX. Purple shows percent error post correction.

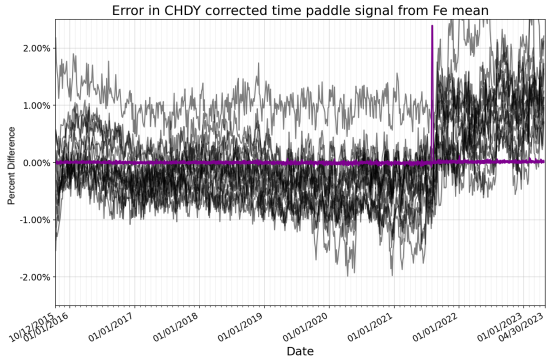

Figure 4(f): Overlay of pre- and post-time corrections for CHDX $_{26}$Fe. Black shows percent error from full layer mean for all paddle means for $_{26}$Fe on CHDY. Purple shows percent error post correction.

itself. When the time corrections are applied to the data set in Figure 4c and 4d, we see that these features can be normalized out of the dataset. The spikes that remain in the data are from the end of July 2021 when ISS was inadvertently rotated by the thrusters of the Nauka module. Data from these timestamps are not correctable and are screened out in the analysis. We can also visualize these corrections as a function of percent error from the full layer mean in Figures 4e and 4f.

3.3 Energy Corrections in Change Assignment

Since the last ICRC, work has continued on the analysis of the subset of data of events that pass through the TASC, which provides each event with energy information. This energy information comes in the form of energy deposited by each individual event. With energy information we can counteract the smearing of charge seen at low energy. While TASC Energy deposited (Edep) is not a one-to-one value with energy, as the efficiency and accuracy are related to charge, it is sufficient to make the corrections we need. Our accuracy in energy determination is excellent for electrons, but as one goes up the periodic table of elements to heavier nuclei, an increasingly significant fraction of the particle shower escapes out of the calorimeter. For events with Z greater than $_{26}$Fe, this means that less than 20% of energy is contained within CALET. To get an exact energy one would use for determining flux, Monte Carlo simulations must be used to unfold the energy. However exact values are not needed to do rudimentary corrections.

We take an initial Tarle charge assignment [6] of CHDX and CHDY to determine the set of candidate $_{26}$Fe events, which is any event within 1-sigma of the $_{26}$Fe peak. From this we divide the full UH TASC subset of events into 65 energy bands each with ~61000 $_{26}$Fe candidate events. We choose to separate these bins by raw Edep rather than by Edep/Z or Edep/nucleon as those alternatives would introduce potential systematic issues that rely on an accurate determination of Z and better understanding of the energy unfolding.

For each energy bin we iterate through the bins performing a multi-Gaussian peak fit on the CHDX (Figure 5a) and CHDY (Figure 5b) event histograms. These plots show an initial charge

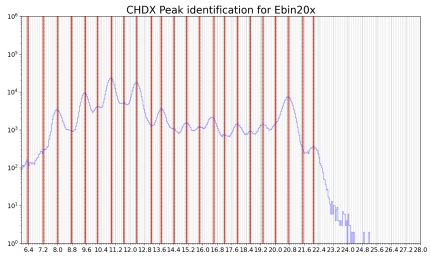

Figure 5(a): Peak identification for CHDX. Blue histogram denotes data, vertical red line denotes the fit routine's guess for peak center. Horizontal axis units are arbitrary based on the square root of CHDX signal.

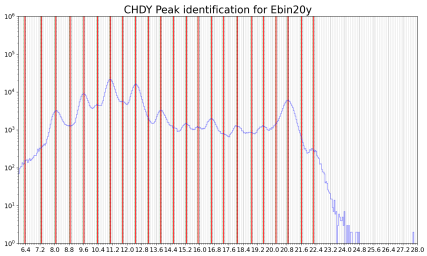

Figure 5(b): Peak identification for CHDY. Blue histogram denotes data, vertical red line denotes the fit routine's guess for peak center. Horizontal axis units are arbitrary based on the square root of CHDY signal.

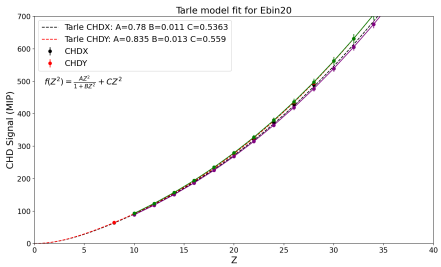

Figure 5(c): Fits to identified peaks in Figure 5a and 5b.

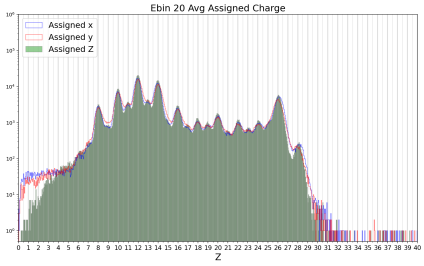

Figure 5(d): Red and Blue lines represent the CHDX and CHDY assigned Z. Green shaded histogram represents the final average of CHDX and CHDY.

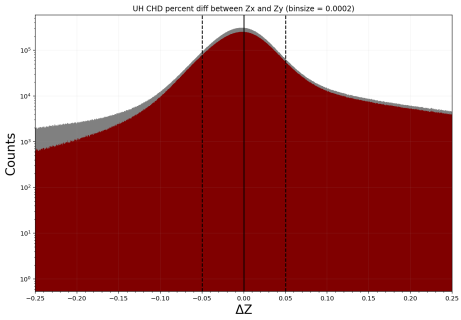

Figure 6(a): Histogram showing percent difference in CHDX and CHDY. All events in gray. Maroon histogram shows events with Edep > 1.535 nmip and not on CHD edge. Binned in 0.02% increments.

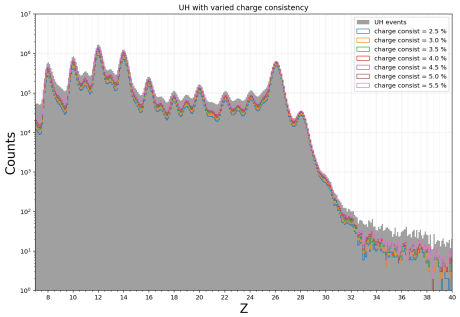

Figure 6(b): Histogram showing how changes in maximum percent difference in charge consistency change relative peak height and peak shape.

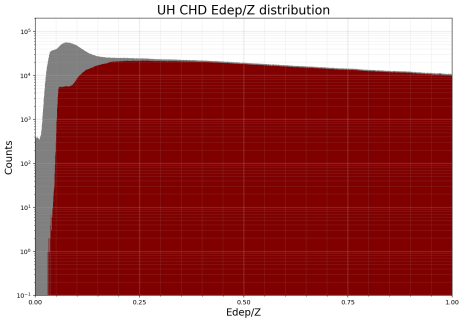

Figure 6(c): Histogram showing how events counts vary with Edep/Z. All events in gray. Maroon histogram shows events with Edep > 1.535 nmip and not on CHD edge. Histogram has a fine binning resolution of 0.005 nmip/Z.

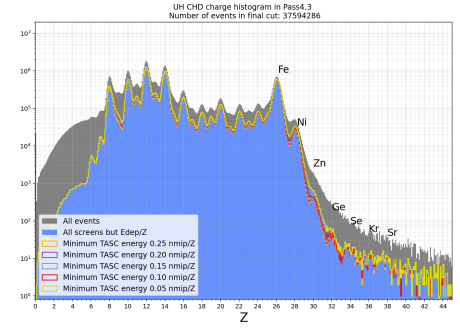

Figure 6(d): Histogram showing how changes in minimum deposited energy change relative peak height and peak shape. Higher energies create clearer peaks at the cost of event count.

based on taking the square root of signal which would corresponds to a Tarle function with A=0 and C=1. From this we can take a multipeak Gaussian fit, initialized with a randomized initial peak height to force peak searching routine to fully explore the parameter space and with bounds of ± 0.15 units on the pseudo-Z scaling. With the identified peak centers, we are able to perform a Tarle model fit to find the actual coefficients of the model.

To constrain this Tarle model fit we scale a region of acceptable fits and expected peak positions for Z>30 by comparing our fit to the ones that were used in the CALET $_{26}$Fe and $_{28}$Ni spectral analyses [4, 5]. This constraint makes sure that our new Tarle functions give reasonable values over the range of energy bins. We also constrain each energy bin by using the previous bin as the initial guess for the fit. This is on both the initial peak fitting and the charge assignment.

4. Screen Selection

As shown in ref. [2], after all corrections are performed we want to perform a small number of event selection screens. This is to remove lower quality events. In the broader analysis we performed cuts for an overall minimum deposited energy and a deposited energy by charge. Additionally, there is a charge consistency cut requiring that the calculated CHD charge for both x and y layers is within 4%. To get to these screens we evaluated the behavior of those quantities as a function of event counts.

The first screen on the lowest three energy bins is not shown here, but was based on the results of the previous energy-based Tarle charge assignment. The lowest three bins suffered from severe smearing of charge and prevent most peaks between $_{14}$Si and $_{26}$Fe from being identified. Since a clean charge assignment could not be done, we screen out those bins.

Figure 6a and 6b show how minor changes in percent difference alter the final histogram. We see that the percent difference is not symmetric, so a good screen needs to occur at value below that asymmetry. The dashed lines added in Figure 6a at ± 0.05% highlight where the asymmetry in CHDX and CHDY approximately begins and constrain the maximum percent difference. Figure 6c and 6d show how Edep/Z behaves. In Fig. 6c, the grey histogram showing all events undergoes a rapid rise into a peak and then has a gradual drop off that becomes approximately linear. The red histogram that omits the first three energy bins, does not have that clear peak but shows a similar linear tapering of event counts. We choose a screen of ~0.15 nmip/Z, so our analysis was past the build-up of events and have both histograms behaving similarly.

5. Conclusions

The effects of these corrections and screens can be seen in ref. [2]. We find them to be an indispensable part of the UH analysis procedure. Future work on improving these corrections would explore into using lower Z peaks for the corrections and potentially requiring more than two peaks. While the screens chosen are effective, research into IMC-based screens could be potentially usable in the full UH-trigger analysis, unlike the TASC screens shown here.

Acknowledgements

We gratefully acknowledge JAXA's contributions to the development of CALET and to the operations onboard the International Space Station. The CALET effort in Italy is supported by ASI under Agreement No. 2013-018-R.0 and its amendments. The CALET effort in the United States is supported by NASA through Grants No. 80NSSC20K0397, No. 80NSSC20K0399, and No. NNH18ZDA001N-APRA18-0004. This work is supported in part by JSPS Grant-in-Aid for Scientific Research (S) Grant No. 19H05608 in Japan.

The material contained in this document is based upon work supported by a National Aeronautics and Space Administration (NASA) grant or cooperative agreement. Any opinions, findings, conclusions, or recommendations expressed in this material are those of the author and do not necessarily reflect the views of NASA.

References

[1] B.F. Rauch et al. (CALET Collaboration), *CALET Ultra Heavy Cosmic Ray Observations on the ISS*, in proceedings of *The 36th International Cosmic Ray Conference*, 2019

[2] W.V. Zober et al. (CALET Collaboration), *Results of the Ultra-Heavy Cosmic-Ray Analysis with CALET on the International Space Station*, in proceedings of *The 38th International Cosmic Ray Conference*, 2023

[3] S. Torii et al. (CALET Collaboration), *Highlights from the CALET observations for 7.5 years on the International Space Station*, in proceedings of *The 38th International Cosmic Ray Conference*, 2023

[4] O. Adriani et al. (CALET Collaboration), *Measurement of the Iron Spectrum in Cosmic Rays from 10 GeV/n to 2.0 TeV/n with the Calorimetric Electron Telescope on the International Space Station* Phys. Rev. Lett. 126, 241101, 2021

[5] O. Adriani et al. (CALET Collaboration), *Direct Measurement of the Nickel Spectrum in Cosmic Rays in the Energy Range from 8.8 GeV/n to 240GeV/n with CALET on the International Space Station* Phys. Rev. Lett. 128, 131103, 2022

[6] G. Tarle, S. P. Ahlen, and B. G. Cartwright. *Cosmic Ray Isotope Abundances from Chromium to Nickel*. ApJ, 230(1979), 607–620.

[7] W.V. Zober et al. (CALET Collaboration), *Progress on Ultra-Heavy Cosmic-Ray Analysis with CALET on the International Space Station*, in proceedings of *The 37th International Cosmic Ray Conference*, 2021

Full Author List: CALET Collaboration

O. Adriani[1,2], Y. Akaike[3,4], K. Asano[5], Y. Asaoka[5], E. Berti[2,6], G. Bigongiari[7,8], W.R. Binns[9], M. Bongi[1,2], P. Brogi[7,8], A. Bruno[10], N. Cannady[11,12,13], G. Castellini[6], C. Checchia[7,8], M.L. Cherry[14], G. Collazuol[15,16], G.A. de Nolfo[10], K. Ebisawa[17], A.W. Ficklin[14], H. Fuke[17], S. Gonzi[1,2,6], T.G. Guzik[14], T. Hams[11], K. Hibino[18], M. Ichimura[19], K. Ioka[20], W. Ishizaki[5], M.H. Israel[9], K. Kasahara[21], J. Kataoka[22], R. Kataoka[23], Y. Katayose[24], C. Kato[25], N. Kawanaka[20], Y. Kawakubo[14], K. Kobayashi[3,4], K. Kohri[26], H.S. Krawczynski[9], J.F. Krizmanic[12], P. Maestro[7,8], P.S. Marrocchesi[7,8], A.M. Messineo[8,27], J.W. Mitchell[12], S. Miyake[28], A.A. Moiseev[29,12,13], M. Mori[30], N. Mori[2], H.M. Motz[31], K. Munakata[25], S. Nakahira[17], J. Nishimura[17], S. Okuno[18], J.F. Ormes[32], S. Ozawa[33], L. Pacini[2,6], P. Papini[2], B.F. Rauch[9], S.B. Ricciarini[2,6], K. Sakai[11,12,13], T. Sakamoto[34], M. Sasaki[29,12,13], Y. Shimizu[18], A. Shiomi[35], P. Spillantini[1], F. Stolzi[7,8], S. Sugita[34], A. Sulaj[7,8], M. Takita[5], T. Tamura[18], T. Terasawa[5], S. Torii[3], Y. Tsunesada[36,37], Y. Uchihori[38], E. Vannuccini[2], J.P. Wefel[14], K. Yamaoka[39], S. Yanagita[40], A. Yoshida[34], K. Yoshida[21], and W.V. Zober[9]

[1]Department of Physics, University of Florence, Via Sansone, 1 - 50019, Sesto Fiorentino, Italy, [2]INFN Sezione di Firenze, Via Sansone, 1 - 50019, Sesto Fiorentino, Italy, [3]Waseda Research Institute for Science and Engineering, Waseda University, 17 Kikuicho, Shinjuku, Tokyo 162-0044, Japan, [4]JEM Utilization Center, Human Spaceflight Technology Directorate, Japan Aerospace Exploration Agency, 2-1-1 Sengen, Tsukuba, Ibaraki 305-8505, Japan, [5]Institute for Cosmic Ray Research, The University of Tokyo, 5-1-5 Kashiwa-no-Ha, Kashiwa, Chiba 277-8582, Japan, [6]Institute of Applied Physics (IFAC), National Research Council (CNR), Via Madonna del Piano, 10, 50019, Sesto Fiorentino, Italy, [7]Department of Physical Sciences, Earth and Environment, University of Siena, via Roma 56, 53100 Siena, Italy, [8]INFN Sezione di Pisa, Polo Fibonacci, Largo B. Pontecorvo, 3 - 56127 Pisa, Italy, [9]Department of Physics and McDonnell Center for the Space Sciences, Washington University, One Brookings Drive, St. Louis, Missouri 63130-4899, USA, [10]Heliospheric Physics Laboratory, NASA/GSFC, Greenbelt, Maryland 20771, USA, [11]Center for Space Sciences and Technology, University of Maryland, Baltimore County, 1000 Hilltop Circle, Baltimore, Maryland 21250, USA, [12]Astroparticle Physics Laboratory, NASA/GSFC, Greenbelt, Maryland 20771, USA, [13]Center for Research and Exploration in Space Sciences and Technology, NASA/GSFC, Greenbelt, Maryland 20771, USA, [14]Department of Physics and Astronomy, Louisiana State University, 202 Nicholson Hall, Baton Rouge, Louisiana 70803, USA, [15]Department of Physics and Astronomy, University of Padova, Via Marzolo, 8, 35131 Padova, Italy, [16]INFN Sezione di Padova, Via Marzolo, 8, 35131 Padova, Italy, [17]Institute of Space and Astronautical Science, Japan Aerospace Exploration Agency, 3-1-1 Yoshinodai, Chuo, Sagamihara, Kanagawa 252-5210, Japan, [18]Kanagawa University, 3-27-1 Rokkakubashi, Kanagawa, Yokohama, Kanagawa 221-8686, Japan, [19]Faculty of Science and Technology, Graduate School of Science and Technology, Hirosaki University, 3, Bunkyo, Hirosaki, Aomori 036-8561, Japan, [20]Yukawa Institute for Theoretical Physics, Kyoto University, Kitashirakawa Oiwake-cho, Sakyo-ku, Kyoto, 606-8502, Japan, [21]Department of Electronic Information Systems, Shibaura Institute of Technology, 307 Fukasaku, Minuma, Saitama 337-8570, Japan, [22]School of Advanced Science and Engineering, Waseda University, 3-4-1 Okubo, Shinjuku, Tokyo 169-8555, Japan, [23]National Institute of Polar Research, 10-3, Midori-cho, Tachikawa, Tokyo 190-8518, Japan, [24]Faculty of Engineering, Division of Intelligent Systems Engineering, Yokohama National University, 79-5 Tokiwadai, Hodogaya, Yokohama 240-8501, Japan, [25]Faculty of Science, Shinshu University, 3-1-1 Asahi, Matsumoto, Nagano 390-8621, Japan, [26]Institute of Particle and Nuclear Studies, High Energy Accelerator Research Organization, 1-1 Oho, Tsukuba, Ibaraki, 305-0801, Japan, [27]University of Pisa, Polo Fibonacci, Largo B. Pontecorvo, 3 - 56127 Pisa, Italy, [28]Department of Electrical and Electronic Systems Engineering, National Institute of Technology (KOSEN), Ibaraki College, 866 Nakane, Hitachinaka, Ibaraki 312-8508, Japan, [29]Department of Astronomy, University of Maryland, College Park, Maryland 20742, USA, [30]Department of Physical Sciences, College of Science and Engineering, Ritsumeikan University, Shiga 525-8577, Japan, [31]Faculty of Science and Engineering, Global Center for Science and Engineering, Waseda University, 3-4-1 Okubo, Shinjuku, Tokyo 169-8555, Japan, [32]Department of Physics and Astronomy, University of Denver, Physics Building, Room 211, 2112 East Wesley Avenue, Denver, Colorado 80208-6900, USA, [33]Quantum ICT Advanced Development Center, National Institute of Information and Communications Technology, 4-2-1 Nukui-Kitamachi, Koganei, Tokyo 184-8795, Japan, [34]College of Science and Engineering, Department of Physics and Mathematics, Aoyama Gakuin University, 5-10-1 Fuchinobe, Chuo, Sagamihara, Kanagawa 252-5258, Japan, [35]College of Industrial Technology, Nihon University, 1-2-1 Izumi, Narashino, Chiba 275-8575, Japan, [36]Graduate School of Science, Osaka Metropolitan University, Sugimoto, Sumiyoshi, Osaka 558-8585, Japan, [37]Nambu Yoichiro Institute for Theoretical and Experimental Physics, Osaka Metropolitan University, Sugimoto, Sumiyoshi, Osaka 558-8585, Japan, [38]National Institutes for Quantum and Radiation Science and Technology, 4-9-1 Anagawa, Inage, Chiba 263-8555, Japan, [39]Nagoya University, Furo, Chikusa, Nagoya 464-8601, Japan, [40]College of Science, Ibaraki University, 2-1-1 Bunkyo, Mito, Ibaraki 310-8512, Japan

PoS(ICRC2023)089